

# Turbulent flow and noise sources on a circular cylinder in the critical regime


Cite as: AIP Advances 9, 085009 (2019); <https://doi.org/10.1063/1.5121544>


Submitted: 04 April 2019 • Accepted: 05 August 2019 • Published Online: 13 August 2019

 Chaofan Zhang (张超凡),  Stéphane Moreau and  Marlène Sanjosé

## COLLECTIONS

Paper published as part of the special topic on [Fluids and Plasmas](#)

 This paper was selected as Featured

 This paper was selected as Scilight



View Online



Export Citation



CrossMark

## ARTICLES YOU MAY BE INTERESTED IN

[Turbulent flow interaction with a circular cylinder](#)

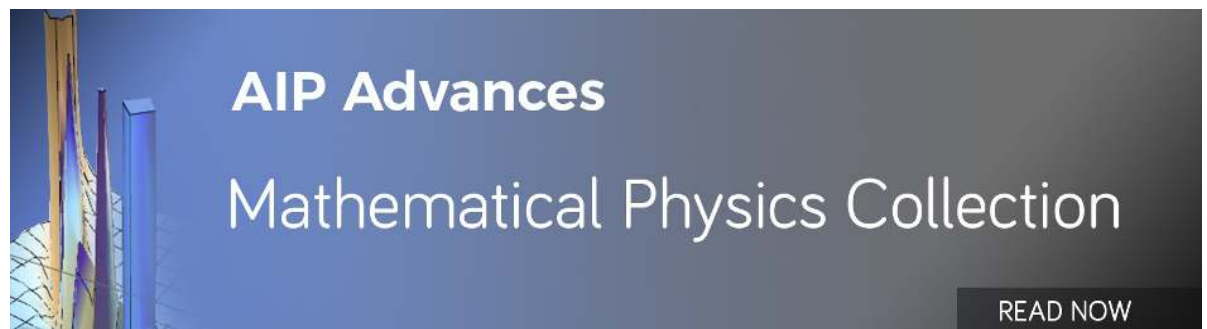
Physics of Fluids **32**, 015105 (2020); <https://doi.org/10.1063/1.5119967>

[Experimental and numerical studies of the flow over a circular cylinder at Reynolds number 3900](#)

Physics of Fluids **20**, 085101 (2008); <https://doi.org/10.1063/1.2957018>

[Numerical studies of flow over a circular cylinder at  \$Re\_D=3900\$](#)

Physics of Fluids **12**, 403 (2000); <https://doi.org/10.1063/1.870318>



AIP Advances  
Mathematical Physics Collection

READ NOW

# Turbulent flow and noise sources on a circular cylinder in the critical regime

Cite as: AIP Advances 9, 085009 (2019); doi: 10.1063/1.5121544

Submitted: 4 April 2019 • Accepted: 5 August 2019 •

Published Online: 13 August 2019



Chaofan Zhang (张超凡),<sup>a)</sup>  Stéphane Moreau,  and Marlène Sanjosé 

## AFFILIATIONS

Department of Mechanical Engineering, Université de Sherbrooke, 2500 Boulevard de l'Université, Sherbrooke, QC J1K2R1, Canada

<sup>a)</sup>chaofan.zhang@usherbrooke.ca

## ABSTRACT

The flow around a circular cylinder with long spanwise length has been investigated in the critical regime using a compressible wall-resolved Large Eddy Simulation (LES) for the first time. The flow at such a critical Reynolds number combines complex features: large favorable and adverse pressure gradient, separation and turbulence transition and flow reattachment. The results of the present simulation agree well with previous experimental and incompressible LES data, for the distribution of the mean wall-pressure coefficient that dominates the drag coefficient, and the skin-friction coefficient that illustrates the flow separation and reattachment behaviors. A weak reattachment is observed from the quasi-zero skin-friction in the reattachment region. A detailed study of the boundary-layer and shear-layer development around the cylinder with profiles of mean velocity and turbulence intensities confirms the transition, separation and reattachment behaviors shown by the skin-friction coefficient. The maximum tangential velocity and its location above the wall have also proven to be adequate measures of the edge velocity and associated boundary layer thickness. The Kelvin-Helmholtz instabilities have been observed in the shear layer and the ratio of the frequency of these instabilities and the fundamental vortex shedding frequency matches well with the existing scaling based on experimental data. The far-field noise obtained by both direct computation and acoustic analogy shows a dominant vortex shedding tone, but with additional broadband sources in the cylinder wake. These sound sources are evaluated from maps of filtered pressure signals and cross-correlation analysis of the pressure fluctuations around the cylinder and in the far-field.

© 2019 Author(s). All article content, except where otherwise noted, is licensed under a Creative Commons Attribution (CC BY) license (<http://creativecommons.org/licenses/by/4.0/>). <https://doi.org/10.1063/1.5121544>

## I. INTRODUCTION

Turbulent flow around a circular cylinder is a classical problem of fluid dynamics for bluff-bodies<sup>1,2</sup> and has wide engineering applications, for instance in transportation systems (train pantograph, automotive axles, aircraft landing gears).<sup>3-5</sup> The flow comprises complex physical features: boundary layer successively subjected to favorable and adverse pressure gradients, flow separation, transition of the shear layer and boundary layer, vortex shedding and turbulent wake containing large structures. The shedding of vortices characterized by a particular Strouhal number  $St_{VK}$  (shedding frequency of the von Kármán street) based on the cylinder diameter  $D$  and the freestream velocity  $u_\infty$  occurs over a wide range of Reynolds numbers and can lead to severe structural vibrations, enhanced mixing, significant increases in the mean drag and high level acoustic noise.<sup>6</sup>

According to Zdravkovich<sup>2</sup> and Achenbach,<sup>7,8</sup> the turbulent flow past a smooth circular cylinder can be divided into four regimes depending on the Reynolds number  $Re_D$  based on  $D$  and  $u_\infty$ :

- Sub-critical regime ( $400 < Re_D < 10^5$ ): the boundary layer is laminar throughout the circumference. Laminar separation occurs at about  $\theta_s = 70^\circ - 80^\circ$  from the forward stagnation point and transition to turbulence occurs in the separated shear layers<sup>9</sup> ( $\theta$  is defined in Fig. 1). The early separation results in a high drag coefficient ( $C_D = 2F_D/\rho_\infty u_\infty^2 A \approx 1.2$ ,<sup>1,10</sup> with  $F_D$  the drag force,  $\rho_\infty$  the free stream density and  $A$  the reference area) that remains quasi-constant. The frequency of the vortex shedding is about  $St_{VK} \approx 0.2$ .<sup>11</sup>
- Critical regime ( $10^5 < Re_D < 3 \times 10^5$ ): it is a range of transition between laminar and turbulent separation. The separation point shifts downstream to about  $\theta_s = 90^\circ$  and at a

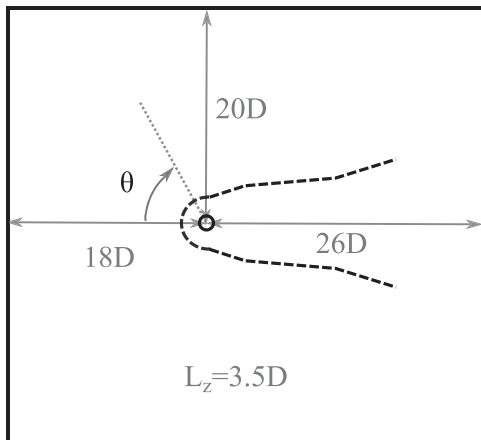


**FIG. 1.** Simulation domain of the cylinder flow: dashed line is the porous FWH-surface.  $\theta$  is the angle from the front stagnation point and equals to  $180^\circ$  at the rear point in the wake.

certain Reynolds number; a laminar separation bubble (LSB) occurs due to the positive pressure gradient; the transition occurs in the shear layer above the LSB and followed by a turbulent reattachment.<sup>8</sup> The shear-layer is closer to the cylinder surface compared with the sub-critical regime. The final separation is located at about  $\theta_s = 130^\circ - 140^\circ$ . The LSB and turbulent reattachment are responsible for the steep drop of drag.<sup>9,12</sup> A sharp increase of the vortex shedding Strouhal number  $St_{VK}$  is also observed. The Reynolds number range of the critical regime is extremely sensitive to the inlet flow conditions.

- Super-critical regime ( $3 \times 10^5 < Re_D < 2 \times 10^6$ ): for smooth surface cylinder, the flow is characterized by an immediate transition from a laminar to turbulent boundary layer downstream of  $\theta = 90^\circ$ . The separation angle reduces from  $\theta_s = 140^\circ$  to  $\theta_s = 120^\circ$ , leading to an increase in the drag coefficient. The vortex shedding Strouhal number is again constant  $St_{VK} \approx 0.45 - 0.5$ .<sup>13,14</sup>
- Trans-critical regime or fully turbulent ( $Re_D > 2 \times 10^6$ ): the transition from laminar to turbulent boundary layer occurs on the front part of the cylinder. The drag coefficient reaches a new plateau lower than in the sub-critical range. The vortex shedding Strouhal number significantly drops.

Note that the flow may be significantly changed and transitions can occur at lower values of  $Re_D$  if surface roughness, vibrations or freestream turbulence are present.<sup>15,16</sup> In the present work, we focus on the cylinder flow in the critical regime. A few experimental studies have been performed at these Reynolds numbers. To examine the boundary layer and the transition to turbulence, Fage and Falkner<sup>10</sup> systematically measured the drag coefficient, the distribution of the mean wall-pressure and the skin-friction coefficient on the cylinder surface. They observed an inflexion point on the mean wall-pressure distribution as the flow enters the critical regime. The transition from laminar to turbulence takes place in the boundary layer near this inflexion point (see for instance Achenbach's measurements<sup>8</sup>). It is now well known that the LSB observed on the cylinder

surface is a characteristic of the critical regime and that its footprint is a plateau in the pressure distribution which is located slightly after the minimum pressure. Tani<sup>12</sup> showed that the LSB above the cylinder surface was similar to that observed on airfoils with incidence. Another interesting feature of the critical regime is the existence of asymmetric flow, where one-side flow separates as in the sub-critical regime and the other side transition takes place above the separation bubble, as observed by Bearman,<sup>9</sup> Achenbach and Heinecke<sup>13</sup> and Schewe.<sup>14</sup> Schewe<sup>14</sup> reported that this asymmetric flow state is stable only for a small range of Reynolds numbers. For sufficiently high Reynolds numbers, the perturbations on both sides of the cylinder yield a nearly symmetric flow behavior with the existence of the LSB on both sides of the cylinder.

Experiments have played a critical role in the understanding of the complex flow around circular cylinders. However, most of them have focused on measuring the global loads, the vortex shedding characteristics and point-wise time-averaged data of the wall-pressure distribution. Besides, the experimental probes can introduce perturbations which can eventually affect the flow regime and the generated sound. Only recently, new experimental methods have been developed to detect sound sources, such as the cross-correlation method<sup>17</sup> that relates the velocity fluctuations measured by Particle Image Velocimetry (PIV) in the wake and the sound pressure fluctuations in the far-field measured with microphones. Oguma *et al.*<sup>18</sup> reconstructed the near-field pressure fluctuations using the velocities measured by PIV coupled with a Poisson equation solver. They then carried out the correlation between this reconstructed near-field and the measured far-field acoustic pressure. However, such a methodology has only been applied to the sub-critical regime. Accurate numerical simulations are then required as they can provide more flow details with constructive insights. Direct numerical simulation (DNS) is the most accurate approach. However it is still limited to low Reynolds number flows due to the large range of scales to be resolved. Only few DNS of the flow around circular cylinders have been achieved up to now. They are mostly two-dimensional (see for instance Inoue and Hatakeyama<sup>19</sup>), and at a maximum Reynolds number  $Re_D = 10000$ , which remains well below the critical regime. Only recently a three-dimensional incompressible DNS was achieved by Dong *et al.*<sup>20</sup> at  $Re_D = 3900/4000$  and  $10000$ . Even though Large eddy simulations (LES) seem to be more affordable to tackle the cylinder flow in the critical regime and beyond, most of them remain in the sub-critical regime.<sup>21–26</sup> Only the incompressible LES by Lehmkuhl *et al.*<sup>27</sup> and Cheng *et al.*<sup>28</sup> cover the present flow range and characterize the flow field in the critical states. Lehmkuhl *et al.*<sup>27</sup> predicted the asymmetric flow behavior for their low Reynolds numbers cases. To the authors' knowledge, they were the first ones to capture this flow feature numerically. Unfortunately, the evolution of the boundary layer and the shear layer were not discussed. Cheng *et al.*<sup>28</sup> focused on the results of the mean wall-pressure and the skin-friction. Only limited discussion on the development of the boundary layer was provided by the evolution of the boundary-layer thickness. Only the mean velocity profiles in the reattached region have been presented for the case with  $Re_D = 3.5 \times 10^5$ . In both above incompressible LES simulations, the study of the sound radiation and its sources was not possible. Moreover, the connection between the development of the boundary layer and the separated shear layer and the noise generation is not yet fully understood. Besides, the detailed noise sources of the

cylinder flow in the critical regime have not yet been studied. Compressible numerical simulation can provide both time-resolved and mean observations of the whole flow field to investigate the link between the boundary layer and the shear layer, and also the analysis of the noise sources. These fundamental results will then be beneficial for the understanding of both aerodynamics and aeroacoustics phenomena on more complex configurations such as the flow around landing gears. As already pointed out by Hutcheson and Brooks,<sup>5</sup> the sub-critical, critical and turbulent states of flow are also the most relevant for landing gear flow applications because of the Reynolds number range involved on its components (struts, cables, axles, and wheels). The selected flow configuration has a Reynolds number,  $Re_D = 2.43 \times 10^5$  in the critical regime, as found on the main leg of the simplified LAGOON landing gear.<sup>29–31</sup> The chosen test condition can then be considered as a key to real world industrial applications.<sup>3,32,33</sup>

The complex flow features around a circular cylinder in the critical regime are thus investigated by a wall-resolved compressible Large Eddy Simulation (LES) for the first time. The numerical method and parameters of this simulation are described in the next section. The flow characteristics at the selected operating condition are investigated in the following section, and compared with previous experimental and numerical studies. The detailed evolution of the boundary layer and the shear layer are then discussed. Finally, the last section considers the analysis of the noise and its sources.

## II. NUMERICAL PARAMETERS

### A. Numerical methods

The spatially filtered LES compressible Navier-Stokes equations that describe the conservation of mass, momentum and energy ( $\rho$ ,  $\rho\mathbf{u}$ ,  $\rho E$ ), are written in the conservative form as:

$$\frac{\partial \mathbf{w}}{\partial t} + \nabla \cdot \mathbf{F}(\mathbf{w}) = 0 \quad (1)$$

where  $\mathbf{w}$  contains conservative variables ( $\rho$ ,  $\rho\mathbf{u}$ ,  $\rho E$ )<sup>T</sup> and the flux tensor  $\mathbf{F}$  can be divided into two parts:

$$\mathbf{F} = \mathbf{F}^c(\mathbf{w}) + \mathbf{F}^v(\mathbf{w}, \nabla \mathbf{w}) \quad (2)$$

where  $\mathbf{F}^c$  is the convective flux depending on  $\mathbf{w}$ ,  $\mathbf{F}^v$  is the viscous flux depending on both  $\mathbf{w}$  and its gradient  $\nabla \mathbf{w}$ . The contributions of the unresolved turbulent scales are included in the viscous flux through the addition of the so called turbulent viscosity or Sub-Grid Scale (SGS) viscosity  $\nu_t$ .<sup>34</sup> The present work uses the Wall-Adapting Local-Eddy model<sup>35</sup> (WALE) to model the turbulent viscosity by

$$\nu_t = (C_w \Delta)^2 \frac{(s_{ij}^d s_{ij}^d)^{3/2}}{(S_{ij} S_{ij})^{5/2} + (s_{ij}^d s_{ij}^d)^{5/4}} \quad (3)$$

where  $S_{ij}$  denotes the tensor of the resolved strain rate,  $C_w = 0.5$  the model constant, and  $\Delta$  the characteristic filter length usually set to be the cube-root of the cell volume.  $s_{ij}^d$  reads

$$s_{ij}^d = \frac{1}{2} (g_{ij}^2 + g_{ji}^2) - \frac{1}{3} g_{kk}^2 \delta_{ij} \quad (4)$$

where  $g_{ij}$  denotes the resolved velocity gradient

$$g_{ij} = \frac{\partial u_i}{\partial x_j} \quad (5)$$

The governing equations are solved by the unstructured compressible LES solver AVBP,<sup>36</sup> using the two-step Taylor-Galerkin finite element scheme TTG4A, which is 4th order in time and 3rd order in space and presents very low dispersion and dissipation.<sup>37–39</sup> Such a numerical methodology has been extensively and successfully used in several previous aerodynamic and aeroacoustic applications.<sup>40–46</sup>

### B. Simulation setup

The diameter of the cylinder is  $D = 0.05$  m, with a uniform inflow of  $u_\infty = 72$  m/s, which leads to a Reynolds number  $Re_D = 2.43 \times 10^5$  at  $T = 293$  K. The reference pressure equals to  $p_\infty = 98900$  Pa. Freestream density and dynamic viscosity equal to  $1.171$  kg/m<sup>3</sup> and  $1.8 \times 10^{-5}$  kg/ms respectively. The computational domain shown in Fig. 1 extends from  $-18D$  to  $26D$  in the streamwise direction and  $-20D$  to  $20D$  in the crosswise direction. The spanwise width is  $3.5D$ , which should be enough according to the experimental data of Schlinker *et al.*<sup>47,48</sup> A hybrid prisms/tetrahedral unstructured grid is used here similarly as Lehmkuhl *et al.*<sup>27</sup> The first prismatic layer of the wall resolved LES (WR-LES) is at least ten times smaller in the wall normal direction compared to previous wall-modeled simulations of the similar flow conditions,<sup>49</sup> and 30 prismatic layers are generated at the wall. In Fig. 2, the grids around the cylinder of the refined mesh are displayed by a crinkle cut view in the mid-span plane. The resulting wall resolution of the wall-resolved LES yields a dimensionless wall distance  $y^+$  mostly near and below 1 with a maximum at 2 as Lehmkuhl *et al.*<sup>27</sup> Similar to the observations reported by Cheng *et al.*,<sup>28</sup> the results of the wall-resolved simulation with similar Reynolds number without additional perturbation are in the sub-critical state. Therefore, two prismatic layers at  $\theta = 72^\circ$  and  $288^\circ$  (total height equals to  $0.04\%D$ ) are removed from the mesh above the cylinder to form two cuboid tripping geometries to introduce disturbances as in the wall-resolved LES of Cheng *et al.*,<sup>28</sup> as shown in Fig. 2. This tripping method stems from the recently proposed methodology for realistic jet noise applications.<sup>46</sup> The final wall-resolved mesh has approximately 160 million cells, which corresponds to about 42 million nodes. For the present wall resolved case, the streamwise and spanwise discretization yield dimensionless grid spacings  $x^+$  and  $z^+$  of about 30, which enables a proper turbulence development.<sup>50</sup> No-slip adiabatic boundary conditions are applied on the cylinder surface, and periodic boundary conditions are imposed in the spanwise direction. Uniform velocity is imposed at the inlet, and Navier-Stokes characteristic non-reflective boundary conditions<sup>51</sup> are used in the far-field, which reduce acoustic reflections.

The time step is fixed to  $\Delta t = 0.2 \times 10^{-7}$  s to ensure an optimized Courant-Friedrichs-Lewy number equal to 0.7 for the TTG4A scheme. The numerical simulation is initialized with homogeneous flow on the coarse mesh. The converged flow results from the coarse mesh is interpolated on the fine mesh as initial solution. After a transient time of 36 ms, a statistically converged flow is achieved and the initial transient is completely washed out of the simulation domain. Statistics are then collected for a physical

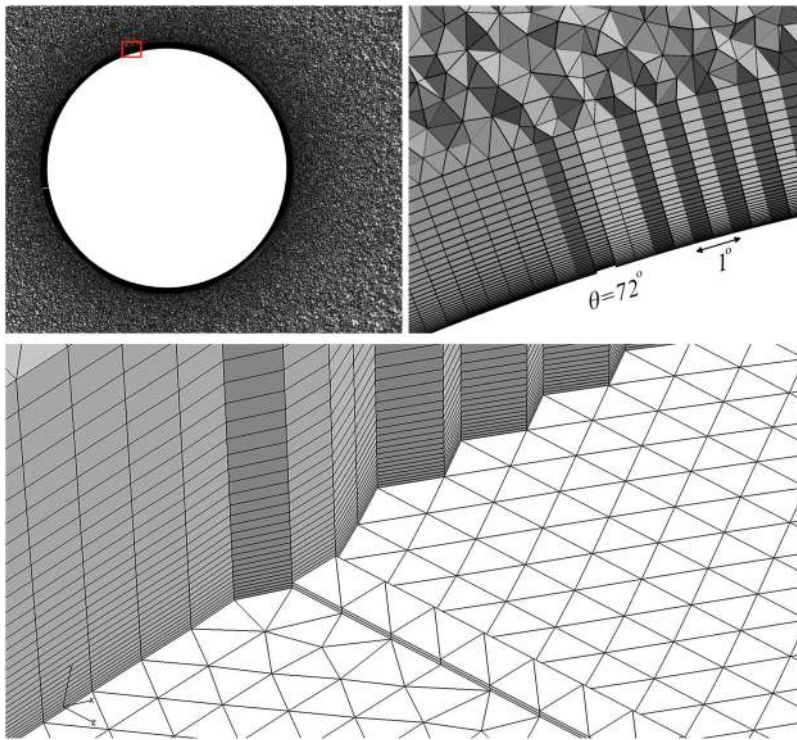


**FIG. 2.** Mesh of cylinder flow in the mid-span plane: top left: mesh around the cylinder; top right: zoom views around  $\theta = 72^\circ$ ; bottom: zoom view around the tripping line near  $\theta = 72^\circ$ .

time of 46 ms, which equals to 65 cylinder-diameter flow-through times or 22 shedding cycles. This physical time also corresponds to the acquisition time for wall-pressure fluctuations as well as for density, velocity, and pressure signals extracted from numerical probes placed in the numerical domain. The computational cost corresponding to the simulated physical time is 1.2 M CPU hours on the Niagara Cluster of Compute Canada using Intel Skylake cores.

**III. RESULTS**

The drag coefficient of the present simulation which results from the wall-pressure and the skin-friction distributions is first compared with several measurements (from Fage and Falkner,<sup>10</sup> Spitzer,<sup>52</sup> Achenbach and Heinecke,<sup>13</sup> Schewe,<sup>14</sup> Bearman,<sup>9</sup> Fujita *et al.*,<sup>15</sup> Hutcheson and Brooks<sup>5</sup> and Vaz *et al.*<sup>53</sup>) and LES results from Lehmkuhl *et al.*<sup>27</sup> and Cheng *et al.*<sup>28</sup> in Fig. 3(a). Within the

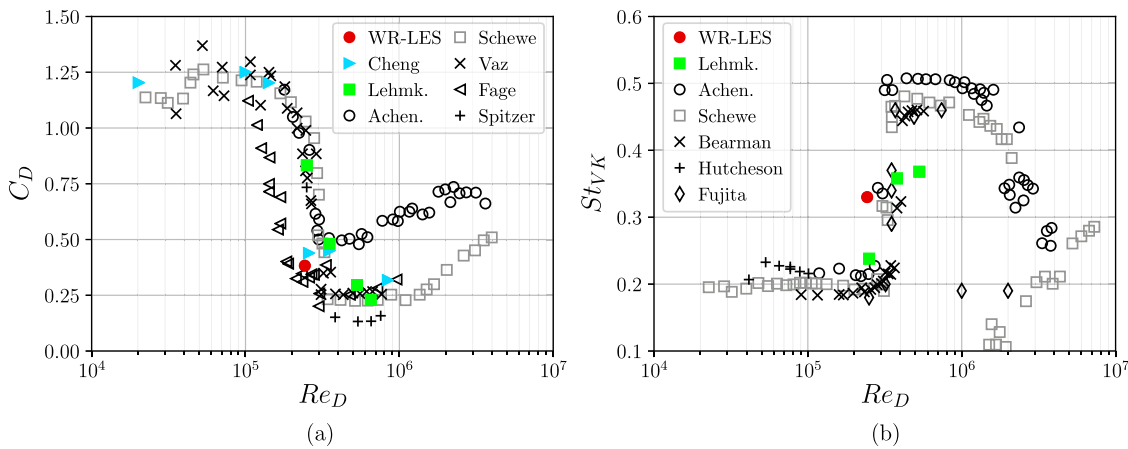


**FIG. 3.** Drag coefficient (a) and Strouhal number (b) as a function of Reynolds number. Comparison of present WR-LES with measurements from Fage and Falkner,<sup>10</sup> Spitzer,<sup>52</sup> Achenbach and Heinecke,<sup>13</sup> Schewe,<sup>14</sup> Bearman,<sup>9</sup> Fujita *et al.*,<sup>15</sup> Hutcheson and Brooks<sup>5</sup> and Vaz *et al.*,<sup>53</sup> LES results Lehmkuhl *et al.*<sup>27</sup> and Cheng *et al.*<sup>28</sup>

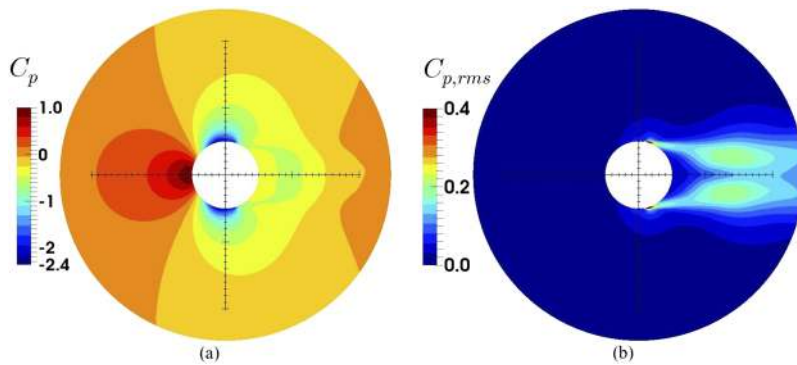


**FIG. 4.** Spanwise averaged mean and root-mean-square pressure fields around the cylinder of the present LES; (a) mean pressure coefficient, (b) coefficient of rms pressure fluctuation.

critical regime, the experimental data show an important scatter due to the aforementioned sensitivity to the flow conditions. The drag coefficient of the present tripped LES is located in the critical regime as expected, within the experimental range. Similarly, the frequency of the vortex shedding varies strongly within the critical regime and the present LES result ( $St_{VK} = 0.33$ ) is close to Achenbach's experimental data, and to Lehmkulh *et al.* LES result but at a higher Reynolds number ( $Re_D = 3.8 \times 10^5$ ).

An overall representation of the mean and fluctuating pressure field is then shown in Fig. 4 in dimensionless forms as pressure coefficients defined as  $C_p = (p - p_\infty)/0.5\rho_\infty u_\infty^2$  and  $C_{p,rms} = p_{rms}/0.5\rho_\infty u_\infty^2$  where  $p_{rms} = (\overline{p^2} - \bar{p}^2)^{0.5}$  ( $\bar{\bullet}$  represents a time averaged quantity) respectively. An almost symmetrical mean static pressure distribution is obtained with a stagnation point near  $\theta = 0^\circ$  (lift coefficient close to zero). The root-mean-square (rms) of the pressure fluctuations are slightly higher on the upper half of the cylinder and two peaks can be seen around the cylinder surface.

### A. Wall pressure and skin friction distribution

The above distribution of pressure around the bluff body (Fig. 4) is not only an important parameter to yield the above drag

and the lift coefficients (Fig. 3), but also the longitudinal pressure gradient is known to affect the development of both laminar and turbulent boundary layers.<sup>55,56</sup> The mean wall-pressure coefficient from the present LES is shown in Fig. 5(a), and is compared with the measurements of Fage and Falkner<sup>10</sup> ( $Re_D = 2.12 \times 10^5$ ), Achenbach<sup>54</sup> ( $Re_D = 2.6 \times 10^5$ ) and the LES of Cheng *et al.*<sup>28</sup> ( $Re_D = 2.6 \times 10^5$  and  $3.5 \times 10^5$ , referred as Cheng-1 and Cheng-2 respectively). The mean wall pressure of present simulation shows a quasi-symmetric distribution on the top and bottom sides of the cylinder. It agrees quite well with all the other data and the plateau between  $90^\circ$  and  $100^\circ$  (also present in Fage's data) is due to a laminar separation bubble (LSB). This plateau caused by the LSB is also observed by Lehmkulh *et al.*<sup>27</sup> within the critical region, on both sides for higher Reynolds numbers ( $Re_D = 5.3 \times 10^5$  and  $6.5 \times 10^5$ ), while for  $Re_D = 2.5 \times 10^5$ , only one side shows the LSB and on the other side, the flow remains in the sub-critical regime. In this asymmetric case, the pressure minimum occurs near  $289.5^\circ$  on the sub-critical regime side, and on the other side of the cylinder presents a deep depression which reaches its minimum at about  $\theta_{C_{p,min}} = 82^\circ$ . A similar position of the minimum pressure is found in the intermediate Reynolds number computed by Lehmkulh *et al.*<sup>27</sup> at  $Re_D = 3.8 \times 10^5$ , which has two slightly asymmetric LSB as observed in the present simulation.

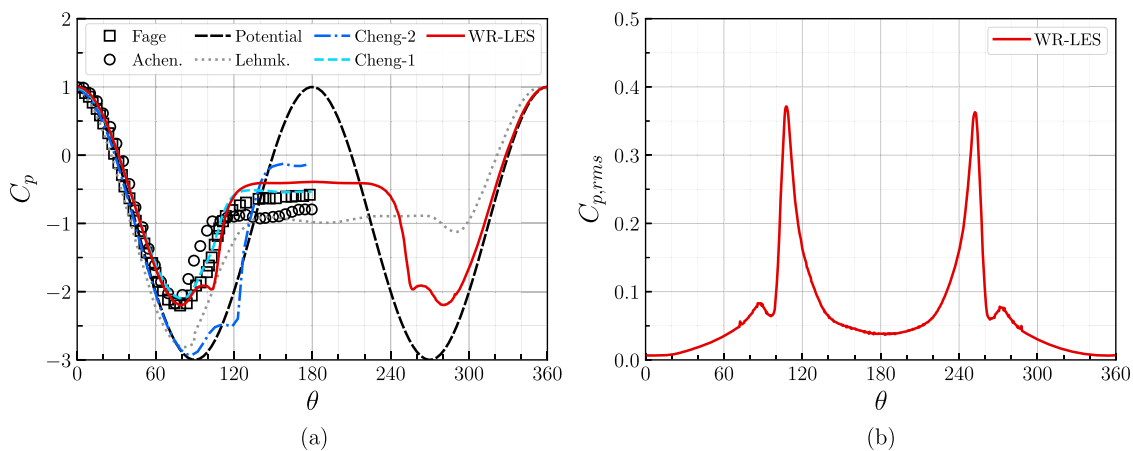


**FIG. 5.** Mean (a) and rms (b) pressure coefficients around the cylinder. Comparison of present simulation with measurements from Fage and Falkner,<sup>10</sup> Achenbach<sup>54</sup> and LES results from Lehmkulh *et al.*<sup>27</sup> and Cheng *et al.*<sup>28</sup>

In the results of Cheng *et al.*<sup>28</sup> with  $Re_D = 3.5 \times 10^5$ , the minimum pressure occurs at  $\theta_{C_{p,\min}} = 88^\circ$ , which is closer to the minimum of the potential flow pressure coefficient,  $C_p = 1 - 4 \sin \theta$ , at  $\theta = 90^\circ$ . Separation then occurs further downstream in this higher Reynolds number case. The corresponding wall-pressure coefficient for the root mean square (rms) of pressure shown in Fig. 4(b), defined as  $C_{p,rms} = p_{rms}/(0.5\rho_\infty u_\infty^2)$ , is depicted in Fig. 5(b). The distribution is slightly asymmetric with different peak values on both sides of the cylinder. The wall-pressure fluctuations which can be seen as the noise sources smoothly increase around the cylinder from the stagnation point until  $90^\circ$  where the laminar separation occurs, then slightly decrease in the separation region up to  $100^\circ$ , and again strongly increase close to the reattachment point of the recirculation bubble at about  $110^\circ$  where the wall-pressure fluctuations show a peak value. This sudden increase of rms pressure is caused by the transition to turbulence of the detached shear layer of the recirculation bubble.

The skin-friction coefficient ( $C_f = \tau_w/0.5\rho_\infty u_\infty^2$ ) is another important parameter that indicates the state of the boundary layer. Indeed, the skin-friction coefficient of a laminar region on a flat plate differs from a turbulent one. In cylinder flows, this parameter has different shapes for different regimes. For example, in the sub-critical regime at  $Re_D = 10^5$ , the skin-friction has a maximum at about  $\theta = 50^\circ$ , and drops rapidly downstream and vanishes at about  $\theta = 80^\circ$ , where the boundary layer separates.<sup>54</sup> In the critical regime, the maximum value rather appears near  $\theta = 60^\circ$  and separation occurs close to  $90^\circ$ . The drop of the skin-friction and the laminar separation in the sub-critical and critical regimes are caused by the adverse pressure gradient.<sup>8</sup> Fig. 6 compares the skin-friction of the present LES with that of Achenbach's measurements at  $Re_D = 2.6 \times 10^5$  and Cheng's LES results. The same increasing skin-friction as in the measurement is obtained from the stagnation point up to about  $\theta = 60^\circ$ , and the experimental rapid drop-off downstream of  $60^\circ$  is nicely recovered. The skin-friction of the present LES also closely follows Cheng's LES results up to  $70^\circ$ . The disturbance between  $70^\circ$  and  $80^\circ$  is caused by the tripping line, which should also be present in Cheng's results. The skin-friction vanishes in the present LES at

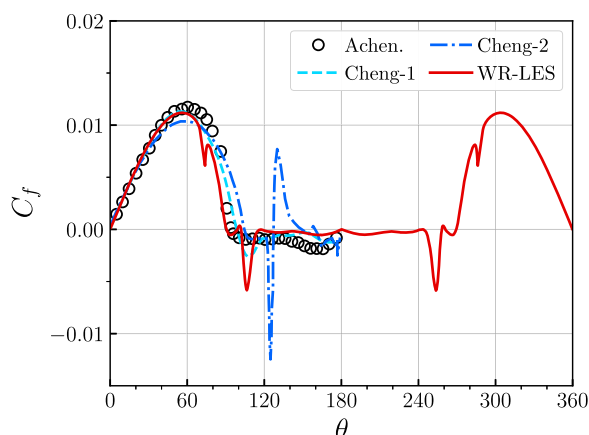


**FIG. 6.** Skin-friction coefficient around the cylinder. Comparison of present simulation with measurements from Achenbach<sup>54</sup> ( $Re_D = 2.6 \times 10^5$ ) and LES results from Cheng *et al.*<sup>28</sup>

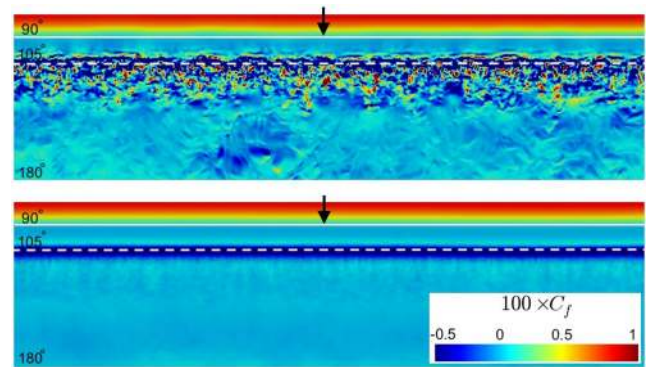


**FIG. 7.** Unwrapped map of an instantaneous (top) and the mean (bottom) skin-friction coefficient from  $90^\circ$  to  $180^\circ$ . White solid and dashed lines indicate the position of  $90^\circ$  and  $105^\circ$  respectively.

$90^\circ$  where the boundary layer separates in a laminar state, which is again close to Achenbach's measurement. In Cheng's LES with  $Re_D = 2.6 \times 10^5$  (Cheng-1), this position is slightly downstream around  $100^\circ$ . After the separation point, from about  $100^\circ$  to  $110^\circ$ , a negative peak appears which indicates the presence of a recirculation bubble, in the same angular range as found by Lehmkühl *et al.*<sup>27</sup> Advancing downstream, the free shear layer becomes turbulent and reattaches at about  $114^\circ$ . There is no positive friction peak created by the weak reattachment, which differs from the higher Reynolds number cases of the critical regime as in Cheng's LES at  $Re_D = 3.5 \times 10^5$  (Cheng-2), or in the LES from Lehmkühl *et al.*<sup>27</sup> (at  $Re_D = 5.3 \times 10^5$  and  $6.5 \times 10^5$ ) and the measurements from Achenbach<sup>8</sup> at  $Re_D = 4 \times 10^5$ . Indeed, Achenbach's measurements have shown that the skin friction peak due to the turbulent reattachment of the boundary layer grows with increasing Reynolds number within the critical flow range. Fig. 7 shows an instantaneous (top) and the mean (bottom) skin-friction coefficient from  $90^\circ$  to  $180^\circ$  along the cylinder span, which confirms the conclusions drawn from Fig. 6. Besides, the laminar separation and transition of the boundary layer can be clearly located in the instantaneous skin friction contours, which can be considered as the footprint of the vortices in the boundary layer. More details about the separation, recirculation and reattachment of the present LES are discussed in the next section.

## B. Boundary layer evolution

Having examined the wall results, the boundary-layer evolution is presented in this section. Boundary-layer behavior is the key factor that determines the flow properties around a cylinder. In Figs. 8, the time and spanwise averaged flow fields near the separation and the recirculation zone of the boundary layer are illustrated by different variables, together with the streamlines. The tangential velocity  $u_\theta$  in Fig. 8(a) confirms that the boundary layer separates (zero and reverse velocity) at about  $90^\circ$ , as also shown by the velocity profiles in Figs. 9. The recirculation bubble mentioned in the previous section from the negative skin friction peak is clearly seen. In the region between  $90^\circ$  and  $100^\circ$ , the recirculation is weak and consequently the skin friction remains close to zero. The reattachment occurs at about  $114^\circ$ . In the reattached region, the tangential velocity near the

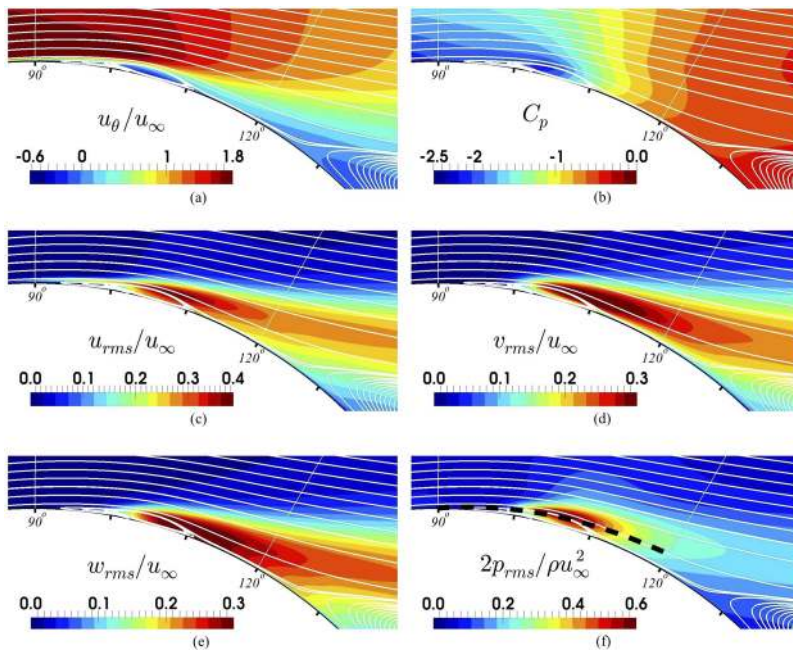


**FIG. 8.** Flow field near the laminar separation bubble (LSB): (a)  $u_\theta$ ; (b) Mean pressure; (c)  $u_{rms}$ ; (d)  $v_{rms}$ ; (e)  $w_{rms}$ ; (f)  $P_{rms}$ , the black-dashed line shows the location of probes in the shear layer from  $90^\circ$  to  $120^\circ$  for every  $2.5^\circ$ .

wall stays close to zero which is confirmed by the tangential velocity profiles in Figs. 9. The velocity gradient in the reattachment region ( $\theta = 115^\circ$  and  $120^\circ$ ) is weak, which is consistent with the above quasi-zero skin friction. The iso-contours of mean static pressure in Fig. 8(b) confirms the plateau on the  $C_p$  curve between  $90^\circ$  and  $105^\circ$ . After  $105^\circ$ , the pressure increases rapidly until the final separation at about  $\theta_s = 130^\circ$  as found by Achenbach.<sup>54</sup> The transition to turbulence of the shear layer is illustrated by the maximum of velocity and pressure fluctuations in Figs. 8 (c–f), immediately after  $100^\circ$ .

The cylinder potential effect prevents an outer uniform flow and the definition of the boundary layer thicknesses requires special care. Therefore, the boundary layer velocity profiles are first normalized by the free-stream velocity  $u_\infty$  and wall normal distance is scaled by the diameter of the cylinder, as plotted in Fig. 9. Before  $80^\circ$ , the pressure gradient is favorable, the boundary flow accelerates and the maximum  $u_\theta$  increases with  $\theta$ . From  $80^\circ$  until the final separation, the maximum tangential velocity decreases from about  $1.8 u_\infty$  to  $u_\infty$ .

Secondly, the radial location of the first maximum value of the tangential velocity  $u_\theta$  is considered as the outer edge of the boundary layer, as in Cheng *et al.*<sup>28</sup> This maximum tangential velocity is denoted as  $u_e$ , which is plotted in Fig. 10(a) and compared with the potential flow velocity and results of Cheng *et al.*<sup>28</sup> at  $Re_D = 3.5 \times 10^5$ . The velocity  $u_e$  of Cheng *et al.*<sup>28</sup> follows the potential flow result up to the separation bubble while in the present LES at lower  $Re_D$ ,  $u_e$  departs from the potential flow gradually and shows a lower maximum value at  $\theta = 80^\circ$ . Cheng's higher value is consistent with the lower pressure coefficient in Fig. 5(a). As expected, the present levels are also larger than those found in the sub-critical regime, which according to Cheng *et al.* all collapse on the curve  $u_e = 1.5 \sin(1.25\theta)$ . Finally, similar plateau as in Cheng's result is observed in the separation bubble region. The velocity profiles normalized by these scales are displayed in Fig. 11. The streamwise pressure

gradient becomes positive after  $80^\circ$ , which thickens the boundary layer significantly, and lifts the mean velocity profiles off the wall till the separation point at  $90^\circ$  (Fig. 10(b)). Polhausen's profiles are also shown for both an attached and a separated cases. They are shown to agree reasonably well with the present results for both flow conditions. The shape factor,  $H$ , which is the ratio between the displacement thickness and the momentum thickness is plotted in Fig. 12(a). It shows a modest increasing trend from the stagnation point around  $\theta = 0^\circ$  to the minimum pressure position at  $\theta_{C_{p,min}} = 82^\circ$ . Beyond this position, a rapid increase of the shape factor is observed. The same conclusion can be drawn from the results of Cheng *et al.*<sup>28</sup> at  $Re_D = 3.5 \times 10^5$ , where the minimum wall pressure is located close to  $\theta = 90^\circ$  and the shape factor increases rapidly after this position, when the adverse pressure gradient starts. In the reattached region ( $114^\circ$  to  $126^\circ$ ) of the present LES,  $H$  shows a value close to 2, which is higher than the typical values of fully developed turbulent boundary layer (TBL) between 1.4 and 1.8.<sup>56</sup> This is again caused by the weak reattachment. In Cheng *et al.*<sup>28</sup>'s results, where a strong reattachment occurs,  $H$  takes a value of about 1.44, which is similar to the one of a flat plate TBL. In both simulations, a second increase of  $H$  is observed after the reattachment where the pressure gradient is adverse.

In Fig. 12(b), the scaled quantity  $Re_{\delta^*}/Re_D^{0.5}$  is compared with the empirical relation  $0.011\theta$ .<sup>5</sup>  $Re_{\delta^*}$  is the Reynolds number based on the displacement thickness as:

$$Re_{\delta^*} = \frac{u_e \delta^*}{\nu} \quad (6)$$

Good collapse between both LES results and the empirical relationship is found up to  $\theta_{C_{p,min}}$ . An rapid increase is observed in both simulations beyond  $\theta_{C_{p,min}}$ .

The rms velocities and turbulent kinetic energy (TKE) between  $80^\circ$  and  $130^\circ$  are plotted in Figs. 13. At  $80^\circ$ , the rms velocities and



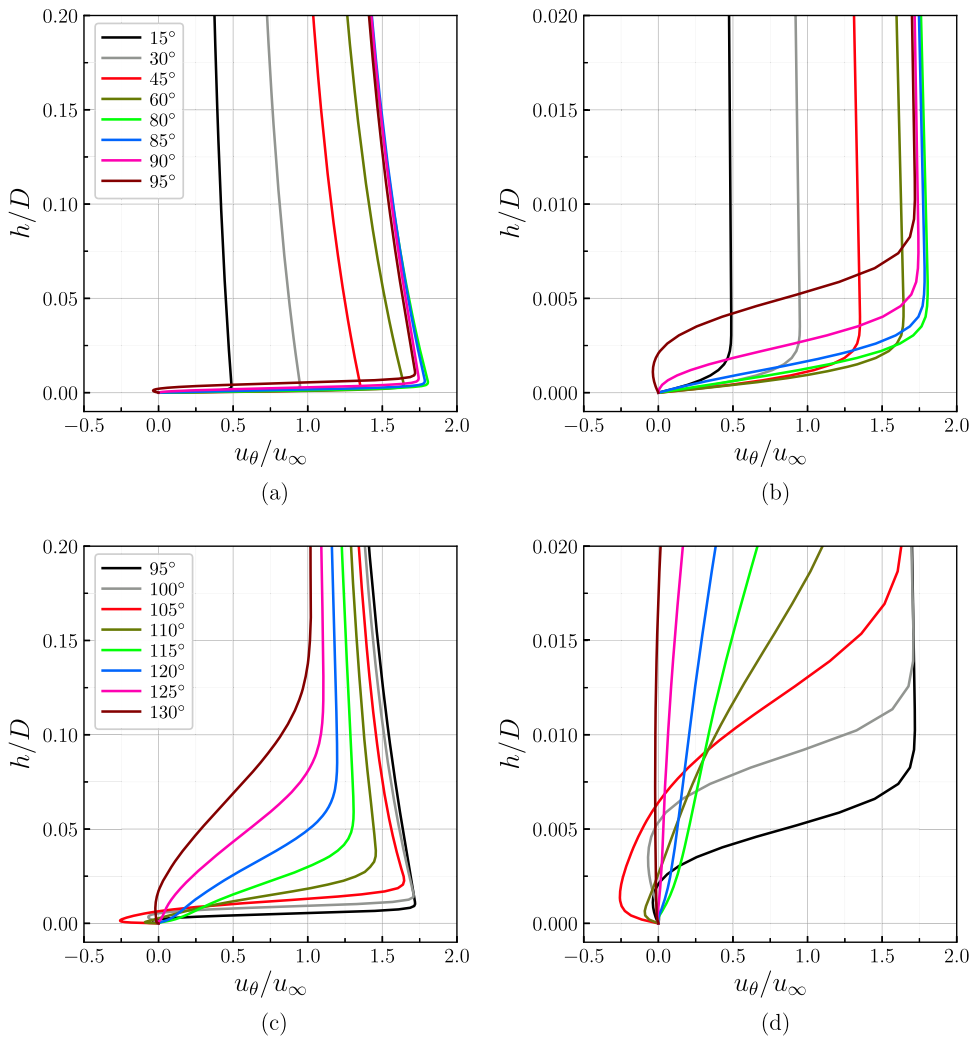


**FIG. 9.** Tangential velocity  $u_\theta$ : (a) full profiles for  $15^\circ \leq \theta \leq 95^\circ$ ; (b) zoomed profile near the wall for  $15^\circ \leq \theta \leq 95^\circ$ ; (c) full profiles for  $95^\circ \leq \theta \leq 130^\circ$ ; (d) zoomed profile near the wall for  $95^\circ \leq \theta \leq 130^\circ$ .

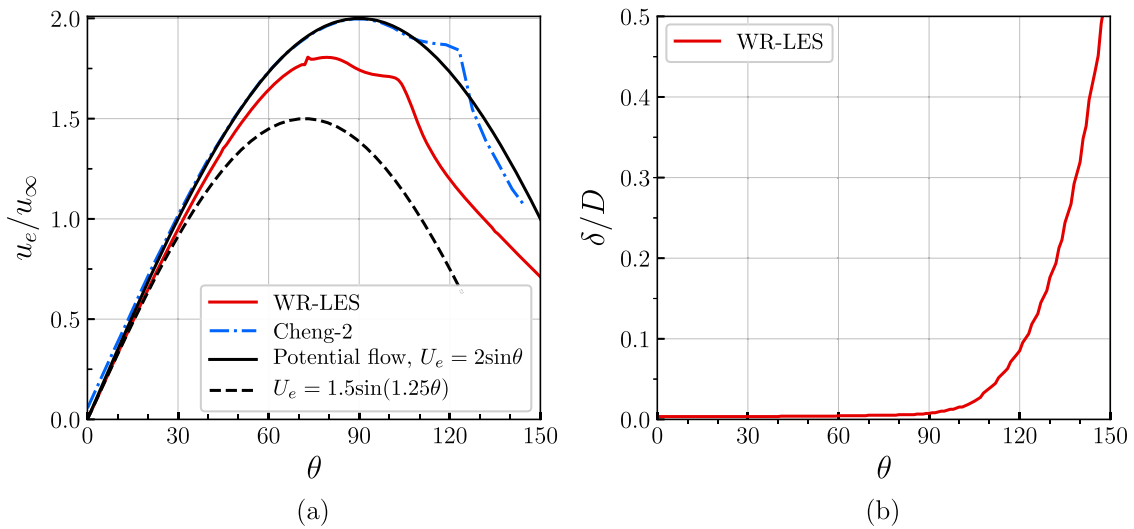


**FIG. 10.** Edge velocity  $u_e$  (a) and boundary layer thickness (b).

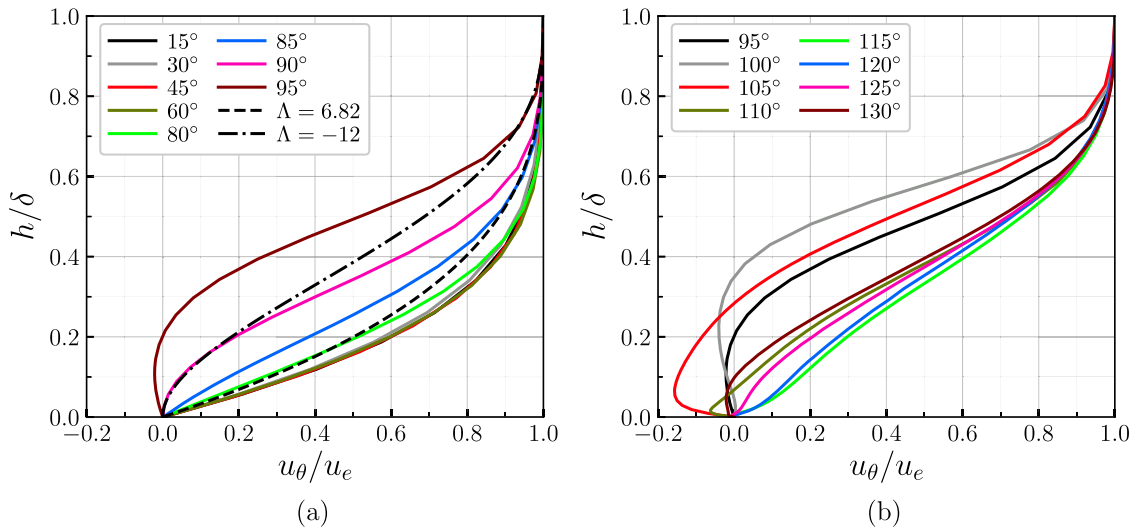


FIG. 11. Tangential velocity profiles normalised by  $u_e$ : (a) for  $15^\circ \leq \theta \leq 95^\circ$ ; (b) for  $95^\circ \leq \theta \leq 130^\circ$ .

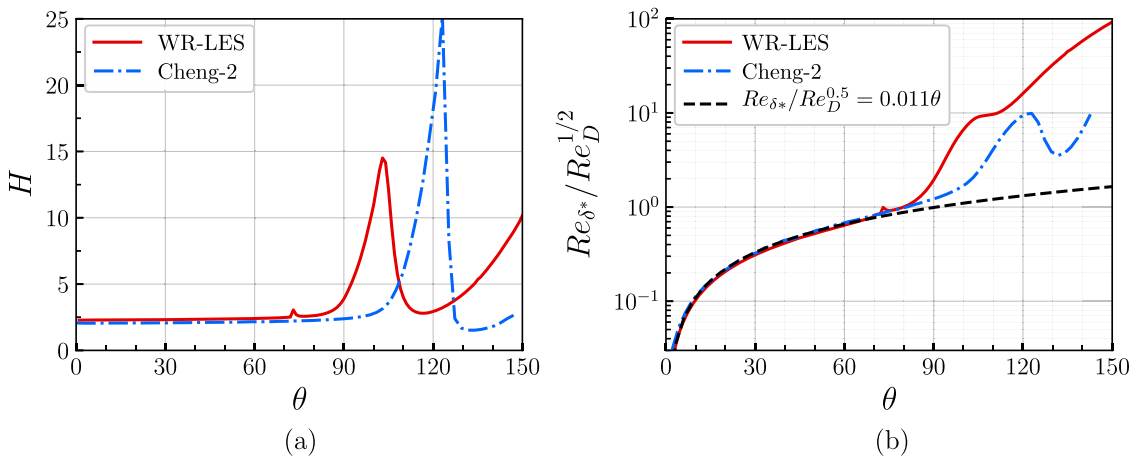


FIG. 12. Global boundary layer parameters: (a) shape factor; (b) distribution of  $Re_{\delta^*}/Re_D^{0.5}$ .

the TKE are small. From the trip, the TKE grows to about 1.3% at the separation point at  $90^\circ$ , and 3% at  $95^\circ$ . A rapid increase can be observed from  $95^\circ$  to  $105^\circ$ , which indicates the transition to turbulence of the shear layer. The maximum TKE is found around  $110^\circ$ . After this angle, the peak value of TKE gradually decreases which is due to the adverse pressure gradient.

### C. Wall and shear-layer pressure spectrum

The PSD of the wall-pressure fluctuations at different angular positions are plotted as a function of the Strouhal number  $St$  based on  $D$  and  $u_\infty$  in Fig. 14. These spectra have been averaged in the spanwise direction. All spectra show a quasi-tonal peak at  $St_{VK} = 0.33$ , which is the fundamental oscillation frequency of the vortex shedding. From  $60^\circ$  to  $105^\circ$ , the fluctuation levels in the

middle and high frequency range increase. Above  $110^\circ$ , these levels decrease.

In addition to the vortex shedding Strouhal number, the wall-pressure spectra can be considered as the footprint of the instability of the shear layer, since the transition occurs shortly after the separation where the shear layer remains close to the cylinder surface. It is known that Kelvin-Helmholtz instabilities in the shear-layer play a key role in the transition to turbulence. These instabilities lead to the formation of small scale vortices which eventually grow up and feed the large scale von Kármán vortex street.<sup>27</sup> The humps in the pressure PSD curves at  $100^\circ$  and  $105^\circ$  at  $St$  between 20 and 30 (the peak frequency denoted as  $St_{KH}$ ) are indeed caused by the Kelvin-Helmholtz instabilities. At  $110^\circ$ , the shear layer becomes fully turbulent and the KH instability hump merges with the turbulent background. These instabilities have been studied back to

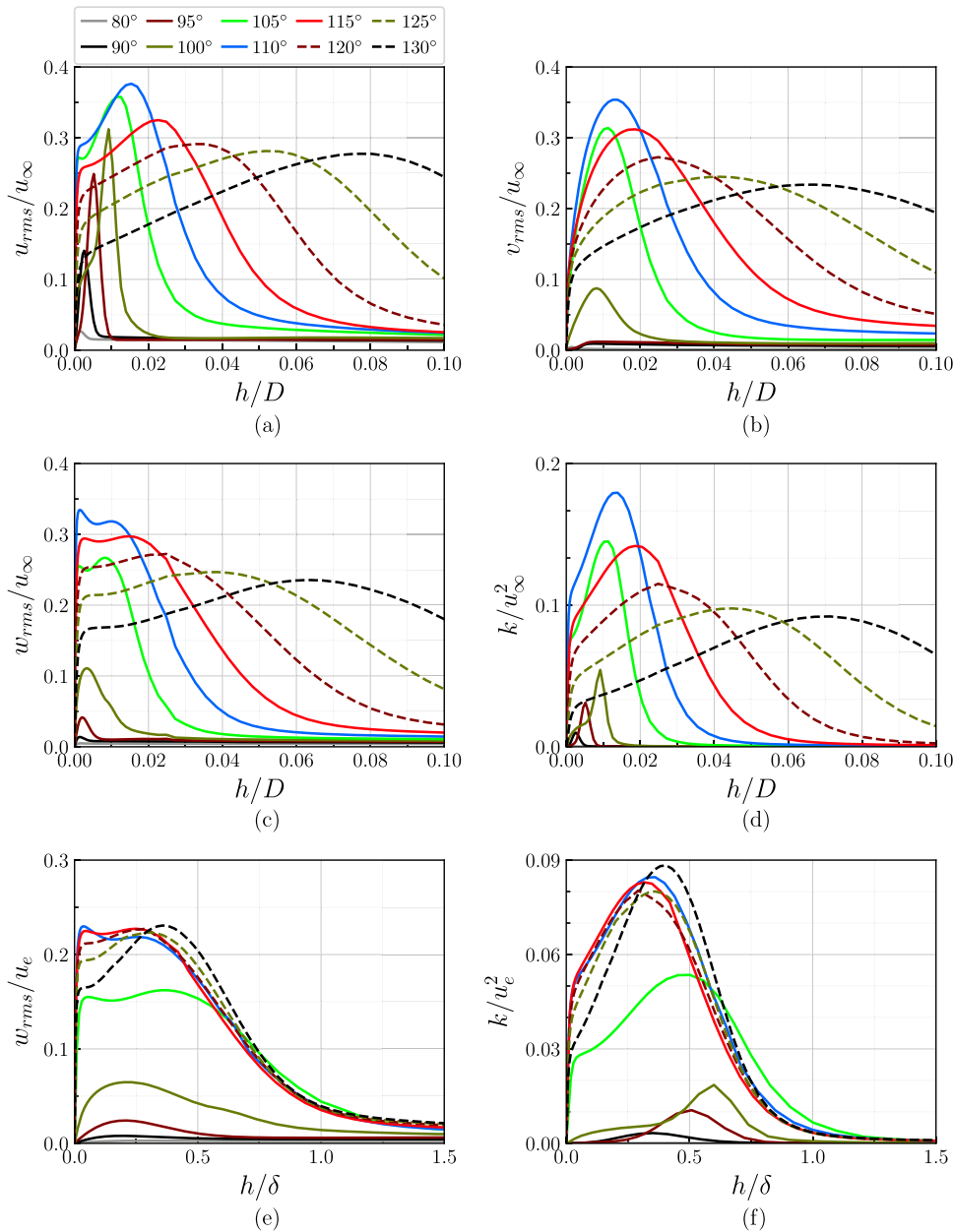


**FIG. 13.** Velocity fluctuations and turbulent kinetic energy profiles: (a)  $u_{rms}$ ; (b)  $v_{rms}$ ; (c)  $w_{rms}$ ; (d)  $k$ ; (e)  $w_{rms}$  using  $\delta$  and  $u_e$  scales; (f)  $k$  using  $\delta$  and  $u_e$  scales.

Bloor,<sup>57</sup> Wei and Smith<sup>58</sup> and Kourta *et al.*<sup>59</sup> The latter suggest a dependency of the ratio  $St_{KH}/St_{VK}$  on the Reynolds number proportional to  $Re_D^{0.5} \approx 493$ , whereas Prasad and Williamson<sup>60</sup> suggest the following expression:  $0.0235 \times Re_D^{0.67} \approx 95$ . The present simulation has  $St_{KH}/St_{VK} \approx 84$ , which is close to these experimental based empirical values. On the curves at 80°, 90° and 95°, some discrete peaks can be observed which are the initial instabilities in the boundary layer and shear layer. Note that no direct measurement of these instabilities has been reported so far for  $Re_D > 10^5$ .

Probes have been placed in the shear layer from 90° to 120°, as shown in Fig. 8(f). Generally, the corresponding spectra of the

crosswise velocity shown in Fig. 15 have similar forms as that of the wall pressure. However, the peaks in the KH instability range from 100° to 107.5° are now comparable or higher than the level near  $St_{VK}$ . The first harmonic of the KH hump is also predicted for the positions from 95° to 102.5°.

Figs. 16(a) and 16(b) show the flow field of the upper shear layer by an iso-surface of the Q-criterion, which is colored by the streamwise velocity. The transition of the separated boundary layer is characterized by the Kelvin-Helmholtz instabilities mainly in the form of rollers stretched in the spanwise direction. Below these structures, the presence of negative spanwise velocity confirms the existence of

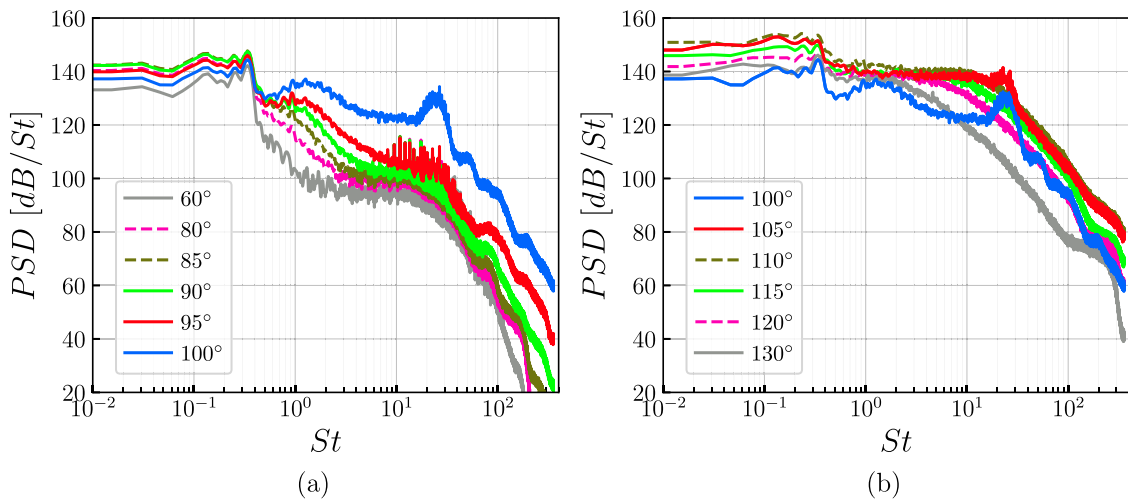


FIG. 14. PSD of the wall-pressure fluctuations.

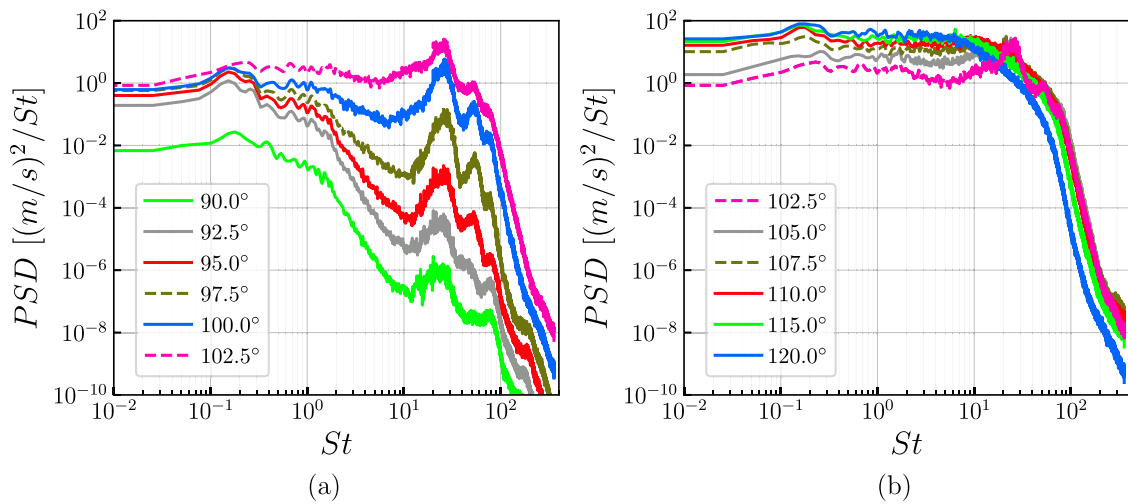


FIG. 15. PSD of the crosswise velocity fluctuations in the shear layer.

the LSB. These initial instabilities develop rapidly into small hairpins. The size of these hairpins increases quickly firstly due to the adverse pressure gradient shortly downstream and then caused by the vortex pairing downstream of the cylinder (after 0.5D).

D. Noise and sources

Flow results, especially the evolution of the boundary layer and shear layer, have been intensively detailed so far, and compared with

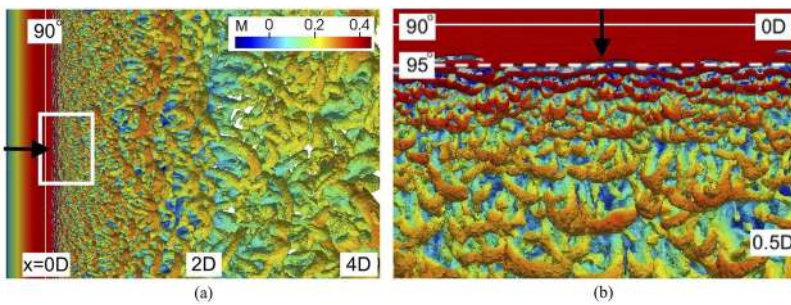
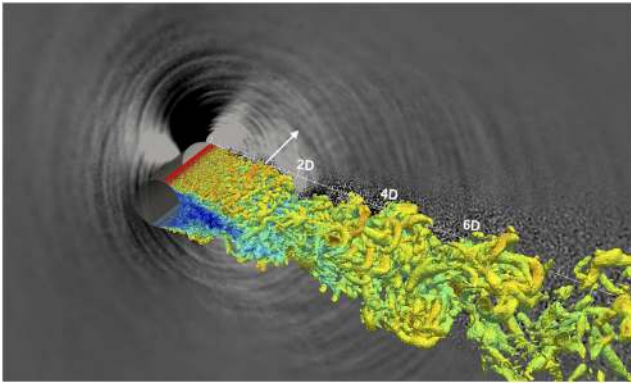


FIG. 16. Iso-surface of Q-criterion from the top of the cylinder colored by the streamwise velocity: (a) view from the top of the cylinder from 0 to 4D; (b) zoom in the white box of (a).



**FIG. 17.** Iso-surface of Q-criterion colored by the streamwise velocity (the same color map as in Fig. 16) with the dilatation field (in gray scale).

**TABLE I.** Recorded temporal signals for the noise source investigation. The vortex shedding period equals 2.1 ms.

Signal length	Sampling frequency	
	$St = 34.7$	$St = 347$
Solid surface	46 ms	32 ms
Porous surface	46 ms	32 ms
Mid-span plane ( $z=0$ )	32 ms	16 ms

previous incompressible simulations. We now focus on the analysis of the noise and its sources entailed by the present compressible LES. Fig. 17 shows the iso-surface of Q-criterion colored by the streamwise velocity with the dilatation in the background. The latter visualizes the sound field around the cylinder. Large low-frequency lobes are first clearly visible, which corresponds to the dominant dipolar vortex shedding tone. The dilatation field then showshigh-frequency

waves mainly centered near  $100^\circ$  where the boundary layer is transitioning to turbulence. Some wave are noticeably radiated from the near shear layer around  $1.5D$  (shown by the white arrow). To investigate the noise and its source, both direct noise computation and Ffowcs Williams and Hawking's (FWH) analogy have been considered for the prediction of the far-field acoustics. The latter and its implementation in the in-house solver sherFWH, has been detailed and validated in Fosso Pouangué *et al.*<sup>40</sup> and Salas and Moreau<sup>61</sup> for instance. Snapshots of the unsteady simulation have been recorded in the mid-span plane of the numerical domain, on the cylinder surface (termed as solid surface) and on a surface surrounding the cylinder and its wake (termed as porous surface as shown by the dashed-line in Fig. 1) every 1000 time-steps and 100 time-steps, resulting in sampling frequencies of  $St = 34.7$  (50 000 Hz) and of  $St = 347$  (500 000 Hz). Modes up to  $St = 17$  and to  $St = 173$  can therefore be obtained respectively. The physical time length of these unsteady signals are given in Table I.

The PSD of the far-field acoustic pressure from both direct simulation and FWH analogy are shown in Fig. 18. The direct simulation results are extracted at  $10D$  above the cylinder ( $\theta = 90^\circ$ ) and have been scaled to  $50D$ , which is the observer position used for the solid and porous FWH analogies. The solid and porous calculations show similar results around  $St_{VK}$ . The direct computation shows slightly higher levels at  $St_{VK}$  and the broadband level in the mid-frequency range agrees well with the porous surface results. The drop at  $St = 4$  in the direct simulation result is caused by the grid cut-off. In the mid-frequency range, both the direct and porous sound levels are higher than the solid ones because of additional noise sources in the cylinder wake. At high frequencies, a broadband hump around  $St = 20$  is shown in both spectra, which is caused by the KH instability and the resulting vortex pairing. Beyond the frequencies of the KH instability, the noise levels drop quickly. Even though these additional noise sources appear, the vortex shedding yielding the aeolian tone at  $St = 0.33$  remains the dominant noise source in this critical regime.

The snapshots of the flow field in the mid-span plane are considered to identify the noise sources. Fourier transforms have been

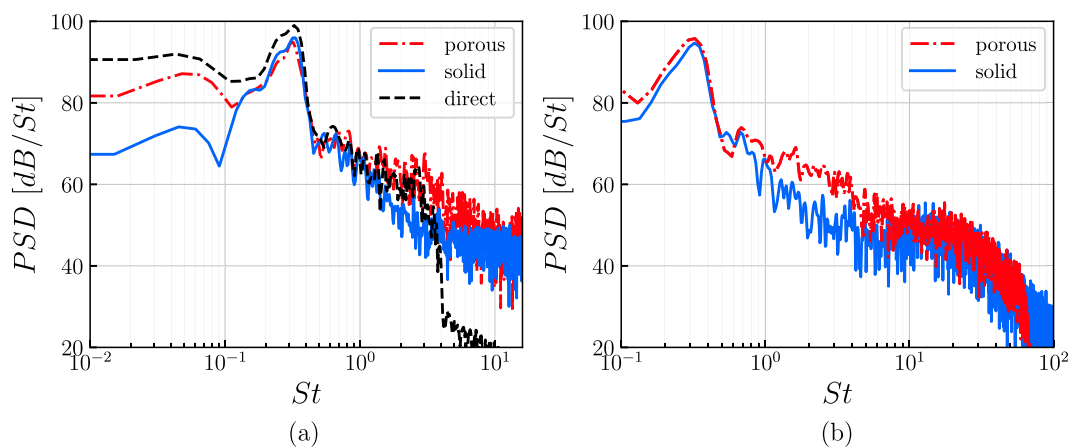


**FIG. 18.** PSD of the far-field acoustic pressure, located at  $90^\circ$   $50D$  above the cylinder, in the  $z=0$  plane: (a) low sampling frequency ( $St = 34.7$ ), the direct result being scaled by the direct acoustic results obtained at  $90^\circ$  located at  $10D$  above the cylinder; (b) high sampling frequency ( $St = 347$ ).

carried out on the time sequence of pressure, crosswise velocity and density at each grid point. The frequency signals are then filtered around  $St = 0.33$  ( $St_{VK}$ ),  $0.66$  ( $2St_{VK}$ ),  $3.0$  (turbulent broadband) and  $26$  (within the KH instabilities). An inverse Fourier transform is performed on these filtered signals to reconstruct the temporal signals. Fig. 19 shows a snapshot of each of these modes. Despite the high intensity of the pressure fluctuations in the shear layer and in the wake, this method is able to clearly capture the propagative sound pressure. In Fig. 19(a), the mode at  $St = St_{VK}$  behaves as a clear lift dipole centered on the final separation position, mostly propagating in the crosswise direction (at  $90^\circ$  and  $270^\circ$ ). As shown in the zoom view in Fig. 19(a), the wave front is born behind the cylinder (solid arrow), and then diffracted by the cylinder into a wave with opposite phase and lobes slightly inclined upstream (dashed arrow).

In Fig. 19(b), for the mode  $2St_{VK}$ , the wavelength decreases to about  $7D$ , and most of the noise radiation occurs in the streamwise direction (drag dipole). The origin of the propagating waves for this mode is slightly shifted downstream in the shear layer at about  $1.5D$  from the center of the cylinder. This explains the higher sound level in the middle frequency range using porous surface compared with the solid surface in Fig. 18. Fig. 19(c) shows the mode at  $St = 3$  in the middle frequency range. The waves for this mode have similar amplitude to the mode  $2St_{VK}$  while their origin is shifted further downstream at about  $2D$ . Fig. 19(d) shows the mode at  $St = 26$ . At this frequency, the wavelength equals roughly  $0.15D$ . The waves are centered at the LSB region on both sides of the cylinder.

Some correlations between the far-field acoustic pressure (at  $10D$  above the cylinder) and the near-field pressure fluctuations in the mid-span plane have been performed, as was done experimentally by Oguma *et al.*<sup>18</sup> in the sub-critical regime ( $Re_D = 40000$ ). They measured the far-field acoustic with microphones and the near-field velocity field using Particle Image Velocimetry (PIV). The near-field pressure was reconstructed using the Poisson equation, which limits this method to incompressible flows. They showed that the peaks of the correlation magnitude were near the separation points (near  $80^\circ$ ) and in the near wake. Fig. 20(a) shows the correlation of the far-field and near-field around the cylinder from the present simulation. Highest peaks are found on the cylinder surface around  $107.5^\circ$  and slightly lower peak levels are located in the near-field shear layer from  $1.0D$  to  $1.8D$ . These features are very similar to the contours of pressure fluctuations in Fig. 4(b). Compared with the sub-critical regime results of Oguma *et al.*,<sup>18</sup> the peak spot near the separation of the critical regime is located closer to the cylinder surface. The correlation between the far-field and the filtered near-field pressure signal around  $St_{VK}$  is shown in Fig. 20(b). The patterns are similar to the one using the complete signal however higher correlation coefficients are observed using the filtered signal at  $St_{VK}$ . The distribution of the correlation coefficients on the cylinder surface is plotted in Fig. 20(c). The correlation increases downstream along the cylinder surface up to the separation point near  $90^\circ$  where a drop occurs caused by the LSB. A clear maximum is observed at  $107.5^\circ$  where the negative peak of the skin-friction coefficient is located and the transition to turbulence of the shear layer occurs.

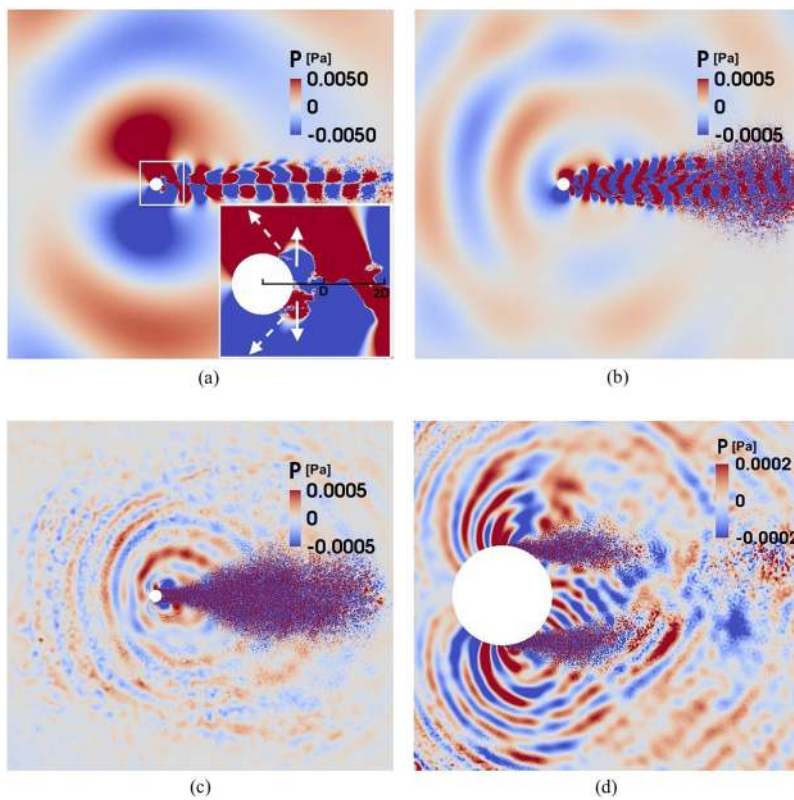
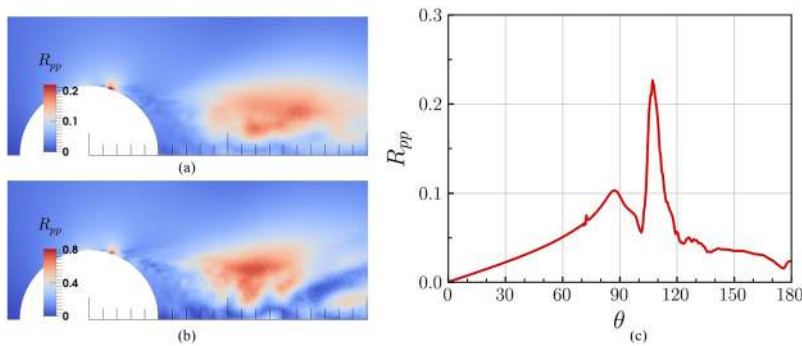


FIG. 19. Filtered pressure fluctuation fields: (a)  $St = St_{VK}$ ; (b)  $St = 2St_{VK}$ ; (c)  $St = 3$ ; (d)  $St = St_{KH}$ .



**FIG. 20.** Correlation of the near-field pressure fluctuations and far-field acoustic pressure (10D above the cylinder): (a) around the cylinder using the complete pressure signal; (b) around the cylinder using filtered pressure signal at  $St_{VK}$ ; (c) distribution on the cylinder surface.

#### IV. CONCLUSIONS

A compressible wall-resolved LES of the flow around a circular cylinder in the critical regime ( $Re_D = 2.43 \times 10^5$ ) has been achieved for the first time using the high-order unstructured solver AVBP. As expected, the flow in this critical regime yields a significant reduced drag compared to the sub-critical cases. The obtained vortex shedding Strouhal number  $St_{VK} = 0.33$  is typical of the critical regime, and lies within the experimental and numerical data range. The mean pressure coefficient and mean skin friction show good agreement with both the previous measurements and incompressible LES references. For instance, the boundary layer displacement thickness and shape factor compare fairly well with Cheng *et al.*<sup>28</sup>'s LES up to the separation using the maximum tangential velocity as boundary layer edge velocity. The latter choice overcomes the difficulty of determining  $u_{95}$  and  $u_{99}$ , and recovers the classical boundary-layer mean velocity and TKE profiles. The boundary layer profiles reveal more details about the flow: strong accelerated profiles are observed up to  $\theta = 80^\circ$  where the static pressure near the wall is the minimum. Above this position, the flow encounters an adverse pressure gradient and some instabilities appear, which are shown by the wall-pressure spectra. However, up to  $90^\circ$ , as shown by the profiles of the TKE for instance, the boundary layer remains rather in a laminar state: the maximum turbulent intensity is less than 0.4%. After  $90^\circ$ , the boundary layer separates on both sides of the cylinder. At the beginning of the flow separation from  $90^\circ$  to  $100^\circ$ , the wall shear stress is nearly zero. At  $95^\circ$  and  $100^\circ$ , the TKE reaches 1% and 2%, and at  $105^\circ$ , this flow parameter reaches 5%, and typical TKE levels of fully turbulent boundary layer are observed from  $110^\circ$  onward, which indicates that the transition to turbulence is complete. The laminar separation and transition in the shear layer are typical features of the critical regime, and the slight flow asymmetry with two LSB is also consistent with the previous incompressible LES results by Lehmkühl *et al.*<sup>27</sup> Yet, the present laminar recirculation bubble with very weak reattachment (quasi-zero shear stress in the reattachment zone), to the authors' knowledge, is observed and reported for the first time both experimentally and numerically.

The wall-pressure spectra confirm the different states of the boundary layer around the cylinder, and additional details have been revealed as well. The footprint of the transition to turbulence triggered by the shear-layer instability close to the cylinder wall has been captured. The  $Q$ -criterion clearly shows that Kelvin-Helmholtz instabilities (rollers) are the main cause of this transition. The corresponding Strouhal number,  $St_{KH} \approx 27$ , is consistent with Prasad

and Williamson<sup>60</sup>'s curve fit of several experimental data at lower Reynolds number  $Re_D$ . To our knowledge, this is another original contribution as no direct measurement of these instabilities have been reported so far for  $Re_D > 10^5$ , and confirms the previous incompressible LES results of Lehmkühl *et al.*<sup>27</sup>

Finally, this compressible LES provides the first insight into the noise sources and associated sound generated by a circular cylinder in the critical regime. The noise sources are qualitatively identified by the filtered time signal of the instantaneous pressure field at different frequencies. The major sources of the far-field sound are also identified by the cross-correlation between the near/far-field pressure fluctuations: the region above the cylinder close to the end of the transition of the shear layer and the shear layer in the near wake are significant additional broadband far-field noise sources in the critical regime. Yet, the dominant noise source remains the vortex shedding, which yields a tone broader and shallower than in previously reported sub-critical cases.

#### ACKNOWLEDGMENTS

The authors acknowledge Compute Canada and Calcul Québec for providing technical support and necessary computational resources for this research. The first author's PhD grant is funded by AIRBUS through the aeroacoustic industrial Chair at Université de Sherbrooke.

#### REFERENCES

- C. H. Williamson, "Vortex dynamics in the cylinder wake," *Annual Review of Fluid Mechanics* **28**, 477–539 (1996).
- M. M. Zdravkovich, *Flow around circular cylinder: Volume 1: Fundamentals* (Oxford University Press, 1997).
- M. Ikeda and T. Mitsumoji, "Evaluation method of low-frequency aeroacoustic noise source structure generated by Shinkansen pantograph," *Quarterly Report of RTRI* **49**, 184–190 (2008).
- W. Wang and S. Watkins, "Reduction of roof rack noise and vibration," *International Journal of Vehicle Noise and Vibration* **6**, 105–117 (2010).
- F. V. Hutcheson and T. F. Brooks, "Noise radiation from single and multiple rod configurations," *International Journal of Aeroacoustics* **11**, 291–334 (2012).
- H. Choi, W.-P. Jeon, and J. Kim, "Control of flow over a bluff body," *Annual Review of Fluid Mechanics* **40**, 113–139 (2008).
- E. Achenbach, "Influence of surface roughness on the cross-flow around a circular cylinder," *Journal of Fluid Mechanics* **46**, 321–335 (1971).
- E. Achenbach, "Total and local heat transfer from a smooth circular cylinder in cross-flow at high Reynolds number," *International Journal of Heat and Mass Transfer* **18**, 1387–1396 (1975).

- <sup>9</sup>P. Bearman, "On vortex shedding from a circular cylinder in the critical Reynolds number regime," *Journal of Fluid Mechanics* **37**, 577–585 (1969).
- <sup>10</sup>A. Fage and V. Falkner, "Further experiments on the flow around a circular cylinder," Reports of the Aeronautical Research Council, London, Reports and Memoranda 1369, 1–13 (1931).
- <sup>11</sup>C. Norberg, "Fluctuating lift on a circular cylinder: Review and new measurements," *Journal of Fluids and Structures* **17**, 57–96 (2003).
- <sup>12</sup>I. Tani, "Low-speed flows involving bubble separations," *Progress in Aerospace Sciences* **5**, 70–103 (1964).
- <sup>13</sup>E. Achenbach and E. Heinecke, "On vortex shedding from smooth and rough cylinders in the range of Reynolds numbers  $6 \times 10^3$  to  $5 \times 10^6$ ," *Journal of Fluid Mechanics* **109**, 239–251 (1981).
- <sup>14</sup>G. Schewe, "On the force fluctuations acting on a circular cylinder in cross-flow from subcritical up to transcritical Reynolds numbers," *Journal of Fluid Mechanics* **133**, 265–285 (1983).
- <sup>15</sup>H. Fujita, H. Suzuki, A. Sagawa, and T. Takaishi, "The aeolian tone characteristics of a circular cylinder in high Reynolds number flow," in *5th AIAA/CEAS Aeroacoustics Conference* (AIAA-99-1849 Paper, Bellevue, WA, 1999).
- <sup>16</sup>H. Fujita, H. Suzuki, A. Sagawa, and T. Takaishi, "The aeolian tone and the surface pressure in high Reynolds number flow," in *6th AIAA/CEAS Aeroacoustics Conference* (AIAA-2000-2002 Paper, Lahaina, HI, 2000).
- <sup>17</sup>A. Henning, K. Kaepernick, K. Ehrenfried, L. Koop, and A. Dillmann, "Investigation of aeroacoustic noise generation by simultaneous particle image velocimetry and microphone measurements," *Experiments in Fluids* **45**, 1073 (2008).
- <sup>18</sup>Y. Oguma, T. Yamagata, and N. Fujisawa, "Measurement of sound source distribution around a circular cylinder in a uniform flow by combined particle image velocimetry and microphone technique," *Journal of Wind Engineering and Industrial Aerodynamics* **118**, 1–11 (2013).
- <sup>19</sup>O. Inoue and N. Hatakeyama, "Sound generation by a two-dimensional circular cylinder in a uniform flow," *Journal of Fluid Mechanics* **471**, 285–314 (2002).
- <sup>20</sup>S. Dong, G. Karniadakis, A. Ekmekci, and D. Rockwell, "A combined direct numerical simulation–particle image velocimetry study of the turbulent near wake," *Journal of Fluid Mechanics* **569**, 185–207 (2006).
- <sup>21</sup>P. Beaudan and P. Moin, "Numerical experiments on the flow past a circular cylinder at sub-critical Reynolds number," Tech. Rep. (Tech. Rep. TF-62, Stanford University, 1994).
- <sup>22</sup>A. G. Kravchenko and P. Moin, "Numerical studies of flow over a circular cylinder at  $Re_D = 3900$ ," *Physics of Fluids* **12**, 403–417 (2000).
- <sup>23</sup>B. Müller, "High order numerical simulation of aeolian tones," *Computers & Fluids* **37**, 450–462 (2008).
- <sup>24</sup>D. A. Lysenko, I. S. Ertesvåg, and K. E. Rian, "Large-eddy simulation of the flow over a circular cylinder at Reynolds number 3900 using the openfoam toolbox," *Flow, Turbulence and Combustion* **89**, 491–518 (2012).
- <sup>25</sup>S. Magne, "Approche numérique du contrôle du bruit tonal des ventilateurs par obstruction de l'écoulement," Ph.D. thesis, Université de Sherbrooke (2015).
- <sup>26</sup>K. Karthik, S. Vengadesan, and S. Bhattacharyya, "Prediction of flow induced sound generated by cross flow past finite length circular cylinders," *The Journal of the Acoustical Society of America* **143**, 260–270 (2018).
- <sup>27</sup>O. Lehmkuhl, I. Rodríguez, R. Borrell, J. Chiva, and A. Oliva, "Unsteady forces on a circular cylinder at critical Reynolds numbers," *Physics of Fluids* **26**, 125110 (2014).
- <sup>28</sup>W. Cheng, D. Pullin, R. Samtaney, W. Zhang, and W. Gao, "Large-eddy simulation of flow over a cylinder with  $Re_D$  from  $3.9 \times 10^3$  to  $8.5 \times 10^5$ : A skin-friction perspective," *Journal of Fluid Mechanics* **820**, 121–158 (2017).
- <sup>29</sup>J.-C. Giret, A. Sengissen, S. Moreau, and J.-C. Jouhaud, "Prediction of LAGOON landing-gear noise using an unstructured LES Solver," in *19th AIAA/CEAS Aeroacoustics Conference* (AIAA 2013-2113 Paper, Berlin, Germany, 2013).
- <sup>30</sup>D. Casalino, A. F. Ribeiro, E. Fares, and S. Nölting, "Lattice-Boltzmann aeroacoustic analysis of the LAGOON landing-gear configuration," *AIAA Journal* **52**, 1232–1248 (2014).
- <sup>31</sup>C. Zhang, "Improvement of wall treatment in large eddy simulation for aeroacoustic applications," Ph.D. thesis, Université de Sherbrooke (2019).
- <sup>32</sup>A. Mohany and S. Ziada, "Flow-excited acoustic resonance of two tandem cylinders in cross-flow," *Journal of Fluid Structure* **21**, 103–119 (2005).
- <sup>33</sup>R. Hanson, A. Mohany, and S. Ziada, "Flow-excited acoustic resonance of two side-by-side cylinders in cross-flow," *Journal of Fluid Structure* **25**, 80–94 (2009).
- <sup>34</sup>P. Sagaut, *Large Eddy Simulation for incompressible flows: An introduction* (Springer-Verlag, New-York, 1998), pp. 1–558.
- <sup>35</sup>F. Nicoud and F. Ducros, "Subgrid-scale stress modelling based on the square of the velocity gradient tensor," *Flow, Turbulence and Combustion* **62**, 183–200 (1999).
- <sup>36</sup>T. Schonfeld and M. Rydgyard, "Steady and unsteady flow simulations using the hybrid flow solver AVBP," *AIAA Journal* **37**, 1378–1385 (1999).
- <sup>37</sup>J. Donea, "A Taylor-Galerkin method for convective transport problems," *International Journal for Numerical Methods in Engineering* **20**, 101–119 (1984).
- <sup>38</sup>O. Colin and M. Rudgyard, "Development of high-order Taylor-Galerkin schemes for LES," *Journal of Computational Physics* **162**, 338–371 (2000).
- <sup>39</sup>J. Donea and A. Huerta, *Finite element methods for flow problems* (John Wiley & Sons, England, 2003).
- <sup>40</sup>A. Fosso Pouangué, M. Sanjosé, S. Moreau, G. Daviller, and H. Deniau, "Subsonic jet noise simulations using both structured and unstructured grids," *AIAA Journal* **53**, 55–69 (2014).
- <sup>41</sup>J.-C. Giret, A. Sengissen, S. Moreau, M. Sanjosé, and J.-C. Jouhaud, "Noise source analysis of a rod-airfoil configuration using unstructured large-eddy simulation," *AIAA Journal* **53**, 1062–1077 (2014).
- <sup>42</sup>P. Salas and S. Moreau, "Direct noise simulation of a canonical high lift device and comparison with an analytical model," *Journal of the Acoustical Society of America* **140**, 2091 (2016).
- <sup>43</sup>T. Leonard, M. Sanjose, S. Moreau, and F. Duchaine, "Large eddy simulation of a scale-model turbofan for fan noise source diagnostic," in *22nd AIAA/CEAS Aeroacoustics Conference* (AIAA Paper, 2016-3000, Lyon, France, 2016), pp. 1–24.
- <sup>44</sup>G. Wang, M. Sanjose, S. Moreau, D. Papadogiannis, F. Duchaine, and L. Gicquel, "Noise mechanisms in a transonic high-pressure turbine stage," *International Journal of Aeroacoustics* **15**, 144–161 (2016).
- <sup>45</sup>C. Zhang, M. Sanjose, and S. Moreau, "Improvement of the near wall treatment in large eddy simulation for aeroacoustic applications," in *2018 AIAA/CEAS Aeroacoustics Conference* (AIAA Paper, 2018-3795, Atlanta, Georgia, 2018), pp. 1–17.
- <sup>46</sup>M. Zhu, C. Pérez Arroyo, A. Fosso Pouangué, M. Sanjosé, and S. Moreau, "Isothermal and heated subsonic jet noise using large eddy simulations on unstructured grids," *Computers & Fluids* **171**, 166–192 (2018).
- <sup>47</sup>R. H. Schlinker and R. K. Amiet, "Vortex noise from nonrotating cylinders and airfoils," in *14th AIAA Aerospace Sciences Meeting* (AIAA Paper 76-81, Washington D.C., 1976).
- <sup>48</sup>M. R. Fink, R. H. Schlinker, and R. K. Amiet, "Prediction of rotating-blade vortex noise from noise of nonrotating blade," Contractor Report CR-2611 (NASA, 1976).
- <sup>49</sup>C. Zhang, M. Sanjosé, and S. Moreau, "Wall-modeled large eddy simulation with adverse pressure gradients: Application to bluff bodies," in *Proceeding of 26th Annual Conference of the CFD Society of Canada* (Winnipeg, Manitoba, Canada, 2018).
- <sup>50</sup>U. Piomelli and E. Balaras, "Wall-layer models for large-eddy simulations," *Annual Review of Fluid Mechanics* **34**, 349–374 (2002).
- <sup>51</sup>T. J. Poinot and S. Lele, "Boundary conditions for direct simulations of compressible viscous flows," *Journal of Computational Physics* **101**, 104–129 (1992).
- <sup>52</sup>R. E. Spitzer, "Measurements of unsteady pressures and wake fluctuations for flow over a cylinder at supercritical Reynolds number," Ph.D. thesis, California Institute of Technology, California (1965).
- <sup>53</sup>G. Vaz, C. Mabilat, R. van der Wal, and P. Gallagher, "Viscous flow computations on smooth cylinders: A detailed numerical study with validation," in *ASME 2007 26th International Conference on Offshore Mechanics and Arctic Engineering* (American Society of Mechanical Engineers, 2007), pp. 849–860.
- <sup>54</sup>E. Achenbach, "Distribution of local pressure and skin friction around a circular cylinder in cross-flow up to  $Re = 5 \times 10^6$ ," *Journal of Fluid Mechanics* **34**, 625–639 (1968).



- <sup>55</sup>F. H. Clauser, "Turbulent boundary layers in adverse pressure gradients," *Journal of Aeronautical Sciences* **21**, 91–108 (1954).
- <sup>56</sup>H. Schlichting, K. Gersten, E. Krause, H. Oertel, and K. Mayes, *Boundary-layer theory* (Springer, 1955), Vol. 7, pp. 1–838.
- <sup>57</sup>M. S. Bloor, "The transition to turbulence in the wake of a circular cylinder," *Journal of Fluid Mechanics* **19**, 290–304 (1964).
- <sup>58</sup>T. Wei and C. Smith, "Secondary vortices in the wake of circular cylinders," *Journal of Fluid Mechanics* **169**, 513–533 (1986).
- <sup>59</sup>A. Kourta, H. Boisson, P. Chassaing, and H. H. Minh, "Nonlinear interaction and the transition to turbulence in the wake of a circular cylinder," *Journal of Fluid Mechanics* **181**, 141–161 (1987).
- <sup>60</sup>A. Prasad and C. H. Williamson, "The instability of the shear layer separating from a bluff body," *Journal of Fluid Mechanics* **333**, 375–402 (1997).
- <sup>61</sup>P. Salas and S. Moreau, "Aeroacoustic simulations of a simplified high-lift device accounting for some installation effects," *AIAA Journal* **55**, 774–789 (2016).